

# Western US intermountain seismicity caused by changes in upper mantle flow

Thorsten W. Becker<sup>1</sup>, Anthony R. Lowry<sup>2</sup>, Claudio Faccenna<sup>3</sup>, Brandon Schmandt<sup>4</sup>, Adrian Borsa<sup>5</sup> & Chunquan Yu<sup>6</sup>

**Understanding the causes of intraplate earthquakes is challenging, as it requires extending plate tectonic theory to the dynamics of continental deformation. Seismicity in the western United States away from the plate boundary is clustered along a meandering, north–south trending ‘intermountain’ belt<sup>1</sup>. This zone coincides with a transition from thin, actively deforming to thicker, less tectonically active crust and lithosphere. Although such structural gradients have been invoked to explain seismicity localization<sup>2,3</sup>, the underlying cause of seismicity remains unclear. Here we show results from improved mantle flow models that reveal a relationship between seismicity and the rate change of ‘dynamic topography’ (that is, vertical normal stress from mantle flow). The associated predictive skill is greater than that of any of the other forcings we examined. We suggest that active mantle flow is a major contributor to seismogenic intraplate deformation, while gravitational potential energy variations have a minor role. Seismicity localization should occur where convective changes in vertical normal stress are modulated by lithospheric strength heterogeneities. Our results on deformation processes appear consistent with findings from other mobile belts<sup>4</sup>, and imply that mantle flow plays a significant and quantifiable part in shaping topography, tectonics, and seismic hazard within intraplate settings.**

Interplate earthquakes are well described by plate tectonics as a consequence of horizontal motion gradients within the surface boundary layer of thermo-chemical mantle convection. For seismicity away from plate boundaries, mantle convection is the fundamental cause as well. However, it is unclear to what extent the location and rate of seismicity is determined by the present-day forcing from active mantle flow, rather than its integrated effect on the buoyancy and rheology of continental lithosphere over geological history. To address this question, we focus on intraplate seismicity in the western US mobile belt, where seismicity and crustal deformation of predominantly extensional style is found around the Snake River plain and Yellowstone hotspot, and following the boundary between the eastern Basin and Range province and the Colorado Plateau further to the south (Fig. 1a–c).

From a lithospheric perspective, lateral variations in density are also expected to have a role in causing seismic strain release. These density variations will lead to lateral variations in gravitational potential energy (GPE; Fig. 1d), that is, the depth-integrated density moment. GPE variations are associated with deviatoric stresses<sup>5</sup> and have been linked with tectonic deformation in the region<sup>6</sup>. Seismicity may further localize at lithospheric strength boundaries, arising from changes in crustal thickness, lithospheric composition, or geotherms<sup>2,3,7</sup>.

Lithospheric heterogeneities evolve over long timescales from mass transport processes associated with plate tectonics and sublithospheric dynamics, including small-scale mantle convection and lithospheric instabilities<sup>7–9</sup>. Present-day active mantle flow may also play a part, and a link between large-scale downwellings and intraplate seismicity was suggested for the 1811/1812 New Madrid ( $M \approx 7$ ) earthquakes, for

example<sup>10</sup>. Advances in structural seismology<sup>3,11,12</sup> now allow calculations of mantle flow on the scales appropriate for our study region<sup>13</sup>. Such models appear to capture deep mantle mass transport<sup>14</sup>, and provide an explanation for anomalous, non-isostatic topography<sup>13,15</sup> (Fig. 1e). The causes for the general state of stress in this part of the North American plate have been explored in numerous studies<sup>16–19</sup>, and geodetically imaged strain-rate patterns in the region have been linked to small-scale mantle flow<sup>8</sup>. However, to our knowledge, no prior geodynamic effort has attempted to predict the spatial distribution of seismicity.

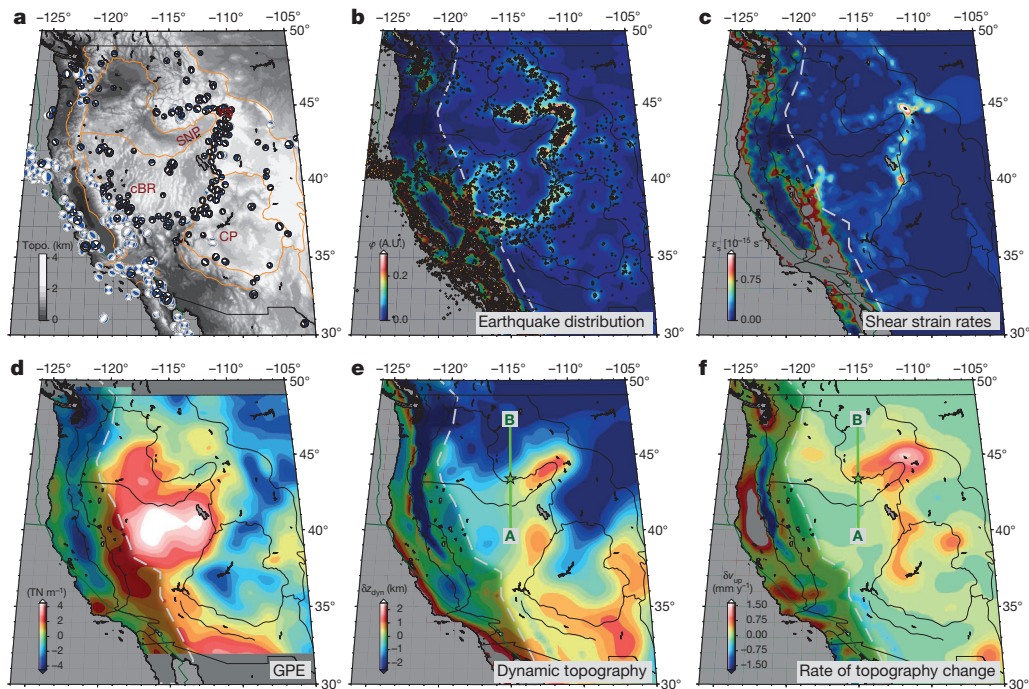
A visual inspection shows an association between seismicity (Fig. 1a, b) and GPE (Fig. 1d), suggesting that lateral gradients in structure are relevant to where earthquakes are found. It is also striking how the rate change of predicted dynamic topography appears to coincide with the regions of intermountain seismicity (Fig. 1f). To quantify these relationships, we computed Molchan error curves<sup>20</sup> (Fig. 2a) and associated skill,  $S$  (Fig. 2b), a statistical metric developed to measure the predictive power of earthquake forecasts<sup>21</sup>. As defined here,  $-0.5 \leq S \leq 0.5$ , with  $S = 0$  for a random forecast and  $S = 0.5$  for a perfect, positive correlation. Actual model skill can be compared with the best case, the seismicity function (Fig. 1b), for which  $S = 0.42$  because of smoothing (Fig. 2a).

Figure 2b shows that lithospheric structure models such as Moho depth and effective elastic thickness, an integral measure of strength, are poor predictors of seismicity, while the two GPE models show significantly positive skill. This implies that seismicity is preferentially found in regions of elevated GPE where an extensional state of stress should be found. When gradients of structural models are considered (Fig. 2b), Moho gradients have small but significantly positive skill, as expected<sup>3,7</sup>. Variations in elastic thickness and GPE model gradients show poor skill.

If we consider mantle flow model predictions, the shear stress amplitude within the viscous flow model's lithosphere is a very poor predictor (Fig. 2b). The vertical normal stress from present-day mantle flow, expressed here as an equivalent ‘dynamic topography’<sup>22</sup> that would be generated in the absence of lithospheric strength and dynamics (Fig. 1e), has a lightly positive  $S$ ; that is, however, not outside the 95% confidence range. In contrast, the inferred rate of change of dynamic topography (Fig. 1f) shows a strong, positive skill of  $S = 0.26$ . This skill is larger than for any of the other models, and is only surpassed by the match of seismicity with the maximum geodetic shear strain rates (Fig. 1c), where  $S$  is of comparable magnitude,  $S = 0.28$ , and Molchan curves have a similar functional form (Fig. 2a). The strong relationship of seismicity to geodetic strain rates is of interest, since geodetic and seismic strain release need not be aligned perfectly throughout the seismic cycle, and aseismic deformation could be decoupled, which (apparently) it is not.

However, crustal deformation forecast skill cannot answer the question about the actual cause of deformation, and only serves as a point of

<sup>1</sup>Department of Earth Sciences, University of Southern California, Los Angeles, California 90089–0740, USA. <sup>2</sup>Department of Geology, Utah State University, Logan, Utah 84322–4505, USA. <sup>3</sup>Department of Sciences, Università Roma Tre, 00146 Roma, Italy. <sup>4</sup>Department of Earth and Planetary Sciences, The University of New Mexico, Albuquerque, New Mexico 87131, USA. <sup>5</sup>Scripps Institution of Oceanography, University of California San Diego, La Jolla, California 92093–0225, USA. <sup>6</sup>Department of Earth, Atmospheric, and Planetary Sciences, Massachusetts Institute of Technology, Cambridge, Massachusetts 02139, USA.



**Figure 1 | Structural and geodynamic maps for the study region.**  
**a**, Topography (Topo.), topographic provinces (orange lines) and focal mechanisms (grey and black from the global Centroid-Moment-Tensor (gCMT)<sup>29</sup> and Saint Louis University<sup>1</sup> catalogues, respectively (gCMT catalogue accessed in December 2014)). cBR, central Basin and Range; CP, Colorado Plateau; SNP, Snake River Plain. **b**, Shallow (depths  $\leq 50$  km) seismicity and

density function,  $\phi$ , A.U., arbitrary units. **c**, Geodetic shear strain rates from GPS<sup>30</sup>. **d**, GPE estimate based on our preferred crustal model<sup>13</sup>. **e**, Dynamic topography inferred from mantle flow<sup>13</sup>. **f**, Rate change of dynamic topography. Shading marked by dashed lines indicates plate boundary regions excluded from most analysis, and **e**, **f**, show the profile used in Fig. 3. See Methods for details.

comparison. Normal geodetic strain rates (Extended Data Fig. 1e) also show positive skill (Fig. 2b), consistent with most events being of extensional character (Fig. 1a). Such a signal in the crust might be expected if an active mantle upwelling (Figs 1f and 3) were to push up and locally extend the lithosphere. (Additional structural models and extension of Molchan analysis to plate boundary seismicity are shown in Extended Data Figs 1–3, and compared with total and wavelength-dependent correlation in Extended Data Figs 4 and 5.)

Inspection of Fig. 1e, f reveals that regions of highest rate of change in dynamic topography correspond to gradients in dynamic topography. The physics of this process can be illustrated by examining mantle flow model profiles across a high seismicity band (Fig. 3). Depending on their buoyancy, upper mantle anomalies produce

upwellings or downwellings (and positive or negative dynamic topography), respectively. However, both types of anomalies can cause positive rate change of dynamic topography, since the upward push of a rising, positive anomaly increases dynamic topography, and the sinking of a negative anomaly reduces negative dynamic topography over time<sup>23,24</sup> (Extended Data Fig. 6). This means that the constructive superposition of anomalies from paired upwellings and downwellings focuses the signal in the intermediate region where most seismicity lies. From Fig. 1e, it appears that mantle upwellings are the main control on the spatial distribution of seismicity in our study region<sup>13,15</sup>. However, the mechanism of change of vertical stressing from mantle flow also applies above downwellings, broadly consistent with earlier work on the New Madrid events<sup>10</sup>, albeit on different spatial scales.

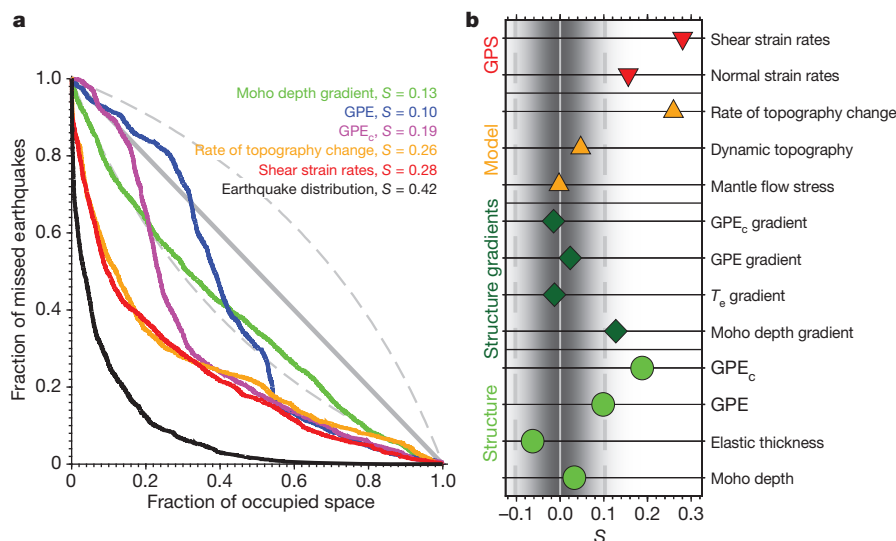


**Figure 2 | Analysis of predictive power for intraplate seismicity.** **a**, Molchan curves<sup>20</sup>, where the diagonal indicates a random prediction, and curves outside the dashed lines are  $\geq 95\%$  significant. **b**, Skill  $S$  (that is, the area above the Molchan curve minus 0.5), where dashed lines indicate the regions outside of which results are 95% significant. We show results from structural models (Moho depth<sup>11</sup>, effective elastic thickness  $T_e$  (ref. 11), and two kinds of GPE models (regular (Fig. 1d) and compensated, GPE<sub>c</sub>), gradients thereof, geodynamic model predictions (compare with Fig. 1e, f) ‘mantle flow stress’, that is, the second invariant of the deviatoric stress), and geodetic models<sup>30</sup> (compare with Fig. 1c). See Methods for details.

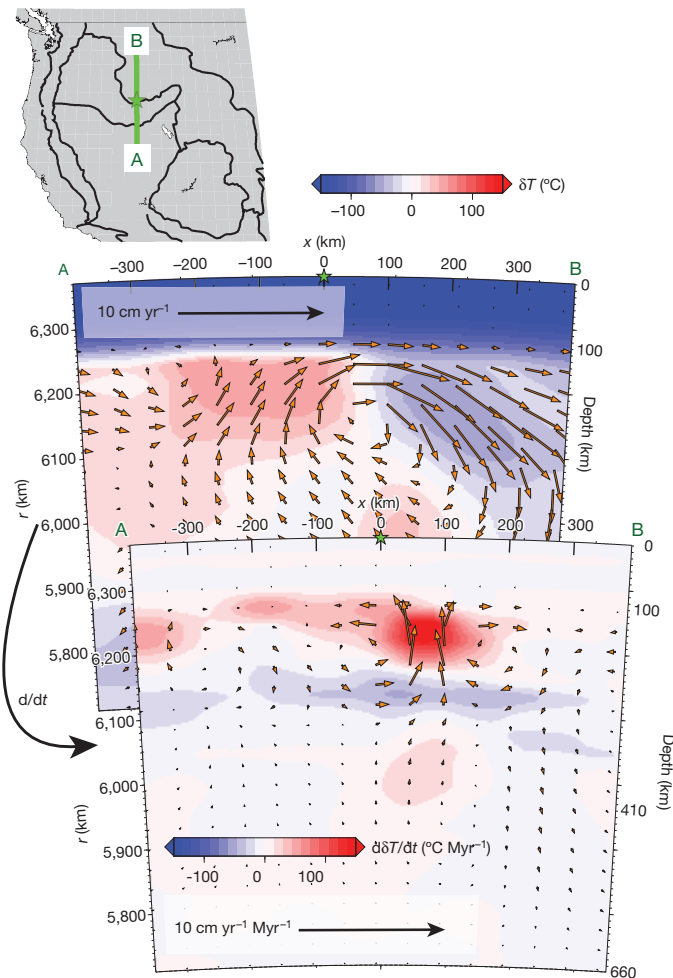


**Figure 3 | Illustration of mantle flow forcing in the study region.** Inferred temperature anomalies and mantle flow velocities (background) and temporal change thereof (foreground) are shown along a north–south profile. Profile location, corresponding dynamic topography, and rate change thereof are shown in Fig. 1e and f, respectively. Also see Extended Data Fig. 6.

Figures 1–3 suggest that the change in vertical normal stresses from mantle convection, coupled with modulation from lithospheric structure, might explain intermountain seismicity. Any such superposition will probably be nonlinear and wavelength dependent in a rheologically complex, visco-elasto-plastically deforming lithosphere. Results from a simplified, linear, multivariable regression imply that both GPE and structural gradients contribute positively, although correlations are improved only moderately relative to that of vertical stressing rates alone (Extended Data Fig. 7). Nonetheless, the physical interpretation of the combined model is appealing: intraplate seismicity responds to changes in vertical stressing rates from mantle flow, and is found in regions with elevated GPE. Moho depth gradients and/or variations in lithospheric thickness then contribute to the localization of seismicity, presumably since zones of lithospheric and crustal weakness lead to locally enhanced strain rates.

Molchan skill or correlation are imperfect metrics of agreement, and even large skill does not imply causality. However, our analysis suggests that intraplate seismicity may be determined by the interplay of active mantle upwellings and lithospheric heterogeneity, reconciling ‘deep’<sup>8,10,13</sup> and ‘shallow’<sup>2,3,6</sup> points of view on the origin of crustal deformation. GPE gradients themselves appear to play a minor part in driving seismicity in this region; rather, high GPE zones seem to mark domains that are buoyed by deep mantle flow<sup>15</sup> and so primed for extensional failure.

A preliminary analysis of geodetically determined vertical motions from Global Positioning System (GPS) data indicates that patterns of surface uplift do not correlate with our predictions of rate change of dynamic topography, except at some wavelengths (Extended Data Fig. 8). This lack of correlation partly stems from neglect of lithospheric strength by the viscous flow model, which would greatly dampen uplift on scales  $\lesssim 200\text{--}600$  km in the region<sup>15</sup>. Effects such as the visco-elastic response to brittle deformation may also contribute strongly to the observed uplift. It is clear that fully resolving the mechanics of intraplate seismicity and topography has to await an integrated mechanical model that can explain a range of data from different disciplines—including geologically constrained uplift—and that improves on rheology and compositional realism. However, improvements in imaging and modelling capabilities, such as those facilitated by EarthScope (<http://www.earthscope.org>), have led to geodynamic models that can already be queried on the relevant scales.

Scenarios involving vertical mantle flow loading and intraplate seismicity may be of global relevance and apply in other mobile belts, such as the Mediterranean–Middle East region, where deformation is diffuse and perhaps related to small-scale convection<sup>4,25</sup>. There, the effect of mantle forcing may also be relevant along complex plate boundaries. An example are the Apennines, where surface deformation appears to be related to changes in dynamic topography<sup>26</sup>, leading to elevated GPE<sup>27</sup>, like in the western United States. This highlights the importance of ongoing mantle convection on sub-plate scales of hundreds to thousands of kilometres, leading to intraplate deformation and seismic activity.

Our analysis suggests that the mantle dynamical perturbation is most important to the deformation behaviour of the crust. Intraplate seismicity may require a disequilibrium perturbation to a system that is already in a critical state of equilibrium stress. This provides a hypothesis for the cause of continental deformation that is quantitatively testable in an increasing number of geographic settings.

**Online Content** Methods, along with any additional Extended Data display items and Source Data, are available in the online version of the paper; references unique to these sections appear only in the online paper.

**Received 1 March; accepted 22 June 2015.**

- Herrmann, R. B., Benz, H. & Ammon, C. J. Monitoring the earthquake process in North America. *Bull. Seismol. Soc. Am.* **101**, 2609–2625 (2011).
- Lowry, A. R. & Smith, R. B. Strength and rheology of the western U.S. Cordillera. *J. Geophys. Res.* **100**, 17947–17963 (1995).
- Levander, A. & Miller, M. S. Evolutionary aspects of the lithosphere discontinuity structure in the western U.S. *Geochem. Geophys. Geosys.* **13**, 1525–2027 (2012).
- Faccenna, C. & Becker, T. W. Shaping mobile belts by small-scale convection. *Nature* **465**, 602–605 (2010).
- Artyushkov, E. V. Stresses in the lithosphere caused by crustal thickness inhomogeneities. *J. Geophys. Res.* **78**, 7675–7708 (1973).
- Jones, C. H., Unruh, J. R. & Sonder, L. J. The role of gravitational potential energy in active deformation in the southwestern United States. *Nature* **381**, 37–41 (1996).
- Bird, P. Lateral extrusion of lower crust from under high topography, in the isostatic limit. *J. Geophys. Res.* **96**, 10275–10286 (1991).
- Fay, N. P., Bennett, R. A., Spinler, J. C. & Humphreys, E. D. Small-scale upper mantle convection and crustal dynamics in southern California. *Geochem. Geophys. Geosys.* **9**, Q08006 (2008).
- van Wijk, J. W. *et al.* Small-scale convection at the edge of the Colorado Plateau: Implications for topography, magmatism, and evolution of Proterozoic lithosphere. *Geology* **38**, 611–614 (2010).
- Forte, A. M., Mitrovica, J. X., Moucha, R., Simmons, N. A. & Grand, S. P. Descent of the ancient Farallon slab drives localized mantle flow below the New Madrid seismic zone. *Geophys. Res. Lett.* **34**, L04308 (2007).
- Lowry, A. R. & Pérez-Gussinyé, M. The role of crustal quartz in controlling Cordilleran deformation. *Nature* **471**, 353–357 (2011).
- Schmandt, B. & Lin, F.-C. P and S wave tomography of the mantle beneath the United States. *Geophys. Res. Lett.* **41**, 6342–6349 (2014).
- Becker, T. W., Faccenna, C., Humphreys, E. D., Lowry, A. R. & Miller, M. S. Static and dynamic support of western U.S. topography. *Earth Planet. Sci. Lett.* **402**, 234–246 (2014).
- Schmandt, B., Jacobsen, S. D., Becker, T. W., Liu, Z. & Dueker, K. G. Dehydration melting at the top of the lower mantle. *Science* **344**, 1265–1268 (2014).

15. Lowry, A. R., Ribe, N. M. & Smith, R. B. Dynamic elevation of the Cordillera, western United States. *J. Geophys. Res.* **105**, 23371–23390 (2000).
16. Flesch, L. M., Holt, W. E., Haines, A. J. & Shen-Tu, B. Dynamics of the Pacific–North American plate boundary in the western United States. *Science* **287**, 834–836 (2000).
17. Humphreys, E. D. & Coblenz, D. North American dynamics and western U.S. tectonics. *Rev. Geophys.* **45**, RG3001 (2007).
18. Forte, A. M., Moucha, R., Simmons, N., Grand, S. & Mitrovica, J. Deep-mantle contributions to the surface dynamics of the North American continent. *Tectonophysics* **481**, 3–15 (2010).
19. Ghosh, A., Becker, T. W. & Humphreys, E. D. Dynamics of the North American continent. *Geophys. J. Int.* **194**, 651–669 (2013).
20. Molchan, G. M. & Kagan, Y. Y. Earthquake prediction and its optimization. *J. Geophys. Res.* **97**, 4823–4838 (1992).
21. Zechar, J. & Jordan, T. Testing alarm-based earthquake predictions. *Geophys. J. Int.* **172**, 715–724 (2008).
22. Richards, M. & Hager, B. H. Geoid anomalies in a dynamic Earth. *J. Geophys. Res.* **89**, 5987–6002 (1984).
23. Gurnis, M., Mitrovica, J. X., Ritsema, J. & van Heijst, H.-J. Constraining mantle density structure using geological evidence of surface uplift rates: the case of the African superplume. *Geochem. Geophys. Geosys.* **1**, 1020 (2000).
24. Conrad, C. P. & Husson, L. Influence of dynamic topography on sea level and its rate of change. *Lithosphere* **1**, 110–120 (2009).
25. Faccenna, C. *et al.* Mantle dynamics in the Mediterranean. *Rev. Geophys.* **52**, 283–332 (2014).
26. Faccenna, C., Becker, T. W., Miller, M. S., Serpelloni, E. & Willett, S. D. Isostasy, dynamic topography, and the elevation of the Apennines of Italy. *Earth Planet. Sci. Lett.* **407**, 163–174 (2014).
27. D'Agostino, N. & McKenzie, D. Convective support of long wavelength topography in the Apennines (Italy). *Terra Nova* **11**, 234–238 (1999).
28. Wessel, P. & Smith, W. H. F. New, improved version of the Generic Mapping Tools released. *Eos Trans. AGU* **79**, 579 (1998).
29. Ekström, G., Nettles, M. & Dziewoński, A. M. The global CMT project 2004–2010: centroid-moment tensors for 13,017 earthquakes. *Phys. Earth Planet. Inter.* **200–201**, 1–9 (2012).
30. Kreemer, C., Blewitt, G. & Klein, E. C. A geodetic plate motion and Global Strain Rate Model. *Geochem. Geophys. Geosys.* **15**, 3849–3889 (2014).

**Acknowledgements** We thank C. Kreemer for publishing his geodetic strain-rate models in electronic form, and C. Conrad for comments. All figures were created with Generic Mapping Tools<sup>28</sup>. Some analysis was based on data services provided by the Plate Boundary Observatory operated by UNAVCO for EarthScope and supported by the National Science Foundation (NSF; EAR-0350028 and EAR-0732947). T.W.B. was partially supported by NSF/US Geological Survey Southern California Earthquake Center, as well as EAR-1215720 and EAR-1215757. A.R.L. was supported by EAR-0955909 and EAR-1358622.

**Author Contributions** T.W.B. conducted the analysis and geodynamic modelling and wrote the paper with A.R.L. T.W.B., A.R.L. and C.F. designed the analysis and contributed to the writing. B.S. and C.Y. advised on geophysical constraints, A.B. provided assistance with GPS data, and all authors collaborated on interpretation of results.

**Author Information** Reprints and permissions information is available at [www.nature.com/reprints](http://www.nature.com/reprints). The authors declare no competing financial interests. Readers are welcome to comment on the online version of the paper. Correspondence and requests for materials should be addressed to T.W.B. ([twb@usc.edu](mailto:twb@usc.edu)).

## METHODS

**Lithospheric structure models.** To address how much of the seismicity patterns (Fig. 1b) can be explained by lithospheric structure and gradients thereof, we mainly consider a Moho depth map and estimates of effective elastic thickness,  $T_e$ , from ref. 11; other Moho maps lead to similar results (Extended Data Fig. 2). Values of  $T_e$  should have some relation to the integrated lithospheric strength, but the driving forces for deformation within the lithosphere should instead be related to the density moment, gravitational potential energy (GPE). We therefore construct a GPE model, integrating our reference crustal model<sup>13</sup> down to an arbitrary compensation depth of  $H = 150$  km. This model is based on crustal density and Moho estimates from ref. 11, and a homogeneous mantle lithosphere. Other crustal models will look similar in terms of GPE<sup>13</sup>.

As expected, the resulting GPE model (Fig. 1d) shares similarities with the corresponding residual (non-Airy) topography<sup>13</sup>, and the main feature away from the plate boundary is the anomalously high GPE within the Basin and Range<sup>6,16</sup>. The step towards relatively low GPE towards the Colorado Plateau corresponds to an increase in crustal thickness towards the east. The broad agreement of this gradient with seismicity patterns motivated the suggestion that lithospheric structure gradients relate to seismicity<sup>2,3</sup>. However, note that in the regions north of the Snake River Plain and Yellowstone, for example, Moho depth gradients are not well aligned with seismicity.

The crustal density model that underpins the GPE model of Fig. 1d is not in isostatic equilibrium, a point that can be interpreted as indicating predominant mantle flow support<sup>13</sup>, or lithospheric compensation<sup>31</sup>. Thus, we also consider a compensated GPE model, GPE<sub>c</sub>, which is constructed by enforcing isostatic balance at  $H$  by allowing arbitrary density anomalies within the mantle lithosphere. GPE<sub>c</sub> has anomaly amplitudes that are subdued by a factor of  $\sim 2$  compared to GPE and looks very similar to other estimates<sup>31</sup>, with the largest anomalies found in the Basin and Range as for GPE.

From all structural models, we also compute the absolute amplitude of the spatial gradient vector. We do so after smoothing each input field with a six standard deviation,  $6\sigma = 100$  km width, Gaussian smoothing kernel.

**Geodynamic models.** Mantle convection models assume a purely viscous, Newtonian rheology and incompressible Stokes flow in the Boussinesq approximation. In line with earlier studies<sup>23,24,32</sup>, the surface boundary conditions are free-slip for computations of dynamic topography, or prescribed plate motions in a North America fixed reference frame, if change in dynamic topography is estimated. This accounts for the effects of relative transport of anomalies by large-scale mantle flow, which only plays a minor part for our study.

The computations here are based on a regional sector of a spherical annulus with horizontal dimensions of  $\sim 7,000$  km  $\times$   $\sim 7,000$  km and 1,200 km depth, computed with a finite element method<sup>33,34</sup>, at half the mesh size ( $\sim 10$  km), but else as in our earlier global models<sup>13,19</sup>. The box size ensures that all results shown here from the centre of the domain are not affected by boundary effects. Dynamic topography results (Fig. 1e), for example, are consistent with those from global computations<sup>13</sup>. Results are also stable with respect to further mesh refinement, and resolution is mainly limited by the structural information from the seismological input models rather than by the numerical methods.

We generally infer mantle temperature (or density) anomalies from the most recent, high-resolution, shear wave,  $v_s$ , tomography model of ref. 12. We first embed this regional model into a global tomographic model<sup>35</sup> to avoid edge effects, and then scale to density  $\rho$ , with a constant conversion factor of  $d \ln \rho / d \ln v_s = 0.2$  below 100 km, for simplicity, as in earlier work<sup>13,14,19</sup>. Scaled temperatures and velocities arise from a Rayleigh number of  $2.3 \times 10^7$ . With a reference viscosity of  $\eta_0 = 10^{21}$  Pa s, the lithosphere (0...100 km), asthenosphere (100...300 km), upper mantle (300...660 km), and lower mantle have viscosities of  $50\eta_0$ ,  $0.1\eta_0$ ,  $\eta_0$  and  $50\eta_0$ , respectively.

For the new rate change of dynamic topography computations, we add a half-space cooling model for the oceanic plate and include lateral lithospheric thickness variations based on inferred LAB thickness<sup>3</sup>. These modifications are intended to improve realism close to the plate boundary; without the modifications, plate boundary proximal regions such as the Cascades show less negative change in dynamic topography (Fig. 1f). However, the modifications have a minor role in shaping rates of change of dynamic topography within the interior plate region, on which our seismicity analysis is focused. Apart from those modifications, the mantle flow models are identical in terms of the approach to our earlier, global mantle flow computations<sup>13,14</sup>, explored with modifications such as anisotropic viscosities in ref. 19.

On the basis of the flow computations, we compute several stress quantities. Stress amplitudes for correlation analysis are obtained from the second invariant of the deviatoric stress tensor at  $\sim 10$  km depth. The instantaneous 'dynamic topography'  $\delta z_{\text{dyn}}$  (Fig. 1e) is computed from the inferred deflections of the surface due to the vertical normal tractions exerted by present-day flow on the top of the

computational domain. Our estimates of dynamic topography here are very similar to those from rheologically simpler models<sup>13</sup>, as expected, since assumptions about density anomalies within the top  $\sim 350$  km are most important for dynamic topography on these scales, and dynamic topography amplitudes scale with density anomalies, to first order.

We also compute the temporal change of  $\delta z_{\text{dyn}}$ , that is, change in mantle-flow-induced vertical normal stress,  $\delta \dot{z}_{\text{dyn}}$ , by taking a finite, forward time derivative between two estimates of  $\delta z_{\text{dyn}}$  after accounting for advection and diffusion of mantle temperature anomalies as well as plate motions for  $\sim 10,000$  years<sup>23,24</sup>. The physics of how different anomalies are expressed as  $\delta z_{\text{dyn}}$  and  $\delta \dot{z}_{\text{dyn}}$  are illustrated in Extended Data Fig. 6 for synthetic anomalies and Fig. 3 for the study region.

Rate change of dynamic topography scales roughly with the density anomalies squared and inversely with asthenospheric viscosity<sup>23</sup>, and those values, their lateral variations, and the general form of the appropriate constitutive relationship, are poorly known. Patterns of  $\delta \dot{z}_{\text{dyn}}$  from flow are therefore much more stable than rates, for a given mantle density distribution, which is why we do not use any absolute amplitude information. The actual geological expression of change in dynamic topography as vertical rock motions will, moreover, be filtered by a range of processes such as erosion, magmatic intrusion, and tectonic shortening or rifting in a rheologically complex lithosphere<sup>36,37</sup>, none of which are considered here.

Predictions from such mantle flow models are expected to be most strongly controlled by the input tomography model. Related differences can be illustrated by considering older models (Extended Data Fig. 9). These lead to flow estimates, and hence conclusions for skill, that are quantitatively different, but qualitatively similar to, those based on our reference model, ref. 12. This is expected because recent, regional tomographic models for the western United States agree in terms of broad velocity anomaly patterns<sup>38</sup>. Moreover, skill is near identical for flow based on the predecessor model for ref. 12, ref. 39 (Extended Data Fig. 9), which was found to best predict seismic delay times<sup>40</sup>. We expect its successor<sup>12</sup> to be even better constrained given that this model was able to rely on a wider aperture data set from EarthScope's USArray.

Another important issue is what assumptions are made regarding the existence of compositional anomalies<sup>13,18,41,42</sup>, which are ignored here besides exclusion of the top 100 km of the lithosphere. This approach is motivated by an encouraging match between dynamic topography from our earlier flow computations and residual surface topography<sup>13</sup> and the overall ability of the flow computations to match large-scale plate motions, the geoid, and deep mass transport<sup>14,19</sup>. We therefore expect the broad patterns of Fig. 1e, f, and the conclusions based on Fig. 2, to be representative of the general expression of mantle flow. However, details of the model predictions may well be subject to further refinement if compositional and partial melt effects on seismic wave speeds, and hence the scaling to temperature, are better constrained.

**Seismicity and Molchan predictive skill.** We base all comparisons of different forward models with seismicity on a merger of all  $M \geq 3$  events in two earthquake catalogues<sup>13,44</sup> that are shallower than 50 km. Our main evaluation of predictive power is based on constructing forecast error curves, typically attributed to Molchan<sup>20</sup>. Such curves can be computed for any scalar field at each instance in time, or for time-independent forecasts, as is done here. The curves are constructed by scanning through the range of represented scalar values of the forecast and plotting, for each value, the fractional number of earthquakes,  $y$ , inside regions where the scalar field is above the current value against the fractional area where scalars are below,  $x$  (Fig. 2a).

A random forecast will plot along the diagonal from  $\{x, y\} = \{0, 1\}$  to  $\{1, 0\}$ , and deviations thereof, for example as measured by the area above the Molchan curve, can be used to quantify predictive power<sup>21</sup>. Here, we define the skill,  $S$ , as that area minus 0.5, such that  $S = 0$  indicates purely random, and the extreme values of  $S = 0.5$  and  $S = -0.5$  perfect correlation and anti-correlation, respectively, in analogy to correlation metrics.

All fields are first smoothed with a  $6\sigma = 100$  km width spatial Gaussian filter before constructing the Molchan curves. We explored other filters as well; while absolute  $S$  values are affected, relative performance of models was found to be similar. We estimate significance from 10,000 Monte Carlo simulations using spatial fields of Gaussian distributed (white noise) random numbers, smoothed in the same way as the actual scalar fields. The corresponding random  $S$  values are found to be approximately Gaussian distributed<sup>21</sup> (grey shading in Fig. 2 and Extended Data Fig. 2), and the  $\sim 95\%$  significance range for our problem can be found outside  $\pm 2\sigma_S$ , with standard deviation of  $\sigma_S \approx 0.05$ .

We consider only seismicity away from the plate boundary for the Molchan curves in Fig. 2 and Extended Data Fig. 2, but Extended Data Fig. 3 shows results including all seismicity of Fig. 1b. For geodetically determined shear strain rates, the skill is larger when plate boundary seismicity is included, increased from  $S = 0.28$  to  $S = 0.35$ . In contrast,  $S$  for the rate change of dynamic topography is

reduced from 0.26 to 0.19 when including the plate boundary. However, this  $S$  value is still larger than for the other models, such as Moho depth gradients (Extended Data Fig. 3). Moreover, the compensated GPE model,  $GPE_c$ , which indicated high skill in Fig. 2 for the intraplate events, loses predictive power when all events are considered:  $S$  is reduced from 0.19 to  $-0.06$ . These findings imply that rate change of dynamic topography may also contribute as a relevant forcing in interplate settings.

**Smoothed seismicity and correlations.** We also compute a seismicity field to estimate a background ‘forecast’ for the Molchan curves, and to use for additional correlation analysis. For this, we sum seismic moments on a  $0.1^\circ \times 0.1^\circ$  grid, take the  $\log_{10}$  of this sum, and then smooth this field with a  $6\sigma = 150$  km width Gaussian filter to define the seismicity density function,  $\phi$ , shown in arbitrary units in Fig. 1b. The skill for this smoothed seismicity field is  $S = 0.42$ , and provides a realistic upper bound for positive correlation forecasts for all scalar fields considered (Fig. 2a and Extended Data Fig. 2).

As for any such study, ‘smoothed seismicity’ maps, like those used for probabilistic forecasting<sup>21</sup>, require choices that influence the scalar fields. Questions arise as to whether to sum magnitudes, number of events, moments, or Benioff strain, and how event kernels should be applied. The Molchan curves are based on individual events and do not suffer from such smoothing assumptions. However, both Molchan curves and smoothed seismicity are affected by earthquake catalogue completeness, which is limited by the duration of the instrumental record, and there will be temporal and spatial changes in completeness. We therefore tried a number of different approaches, but ended up with that of Fig. 1b, where the  $\phi$  scalar field appears to be a good approximation of the spatial distribution of seismicity (Fig. 1a, b). Other choices for generating  $\phi$  would lead to quantitatively different, but qualitatively similar results.

Extended Data Fig. 4 shows additional correlation,  $r$ , analysis based on smoothed seismicity. For this, we use an even-area regional sampling of  $\phi$  and all scalar fields considered. As for the Molchan analysis, all fields are first smoothed with a  $6\sigma = 100$  km spatial Gaussian filter, and statistical significance is estimated from 10,000 Monte Carlo simulations. We find a standard deviation for the random correlations of  $\Sigma_r \approx 0.04$ , and roughly normally distributed values. Extended Data Fig. 4 shows the  $\pm 2\Sigma_r$  range outside which correlation would be inferred to be  $\sim 95\%$  significant. We also conducted a shift test, displacing the rate of topography change field in a random direction by a distance of between 250 and 1,000 km and recomputing correlation with seismicity. From those tests, correlations of  $|r| \geq 0.2$  and  $|r| \geq 0.3$  are estimated to be 96% and 99.8% significant, respectively.

Extended Data Figure 4 indicates that Pearson correlation coefficient,  $r$ , results are very consistent with the relative model performance as indicated by the Molchan scores (Extended Data Fig. 2). We explored different smoothing, while absolute  $r$  values are affected, relative performance of models was found to be similar, as for  $S$ . For example, if we repeat the exercise of Extended Data Fig. 4 using a 250 km rather than 100 km Gaussian smoothing,  $|r|$  is increased by  $\sim 0.05$ , but for all models by roughly the same amount.

Extended Data Figure 5 explores wavelength dependence of correlation further using sliding band-pass filtering, with details described in ref. 13. We find that the general wavelength-dependent behaviour is similar for both linear,  $r$ , and Spearman rank correlation,  $r_s$ , which provides confidence in the overall match between the signals. However, detailed variations, particularly for wavelengths  $\leq 400$  km, are dependent on the type of correlation metric used. This indicates that total correlations in Extended Data Fig. 4 emphasize the differences between  $r$  and  $r_s$  by integration. It also implies that relatively small spatial scales are where neglected effects, such as the flexural rigidity of the lithosphere, and artefacts due to filtering, may predominantly complicate correlation analysis. However, the general wavelength dependence is irrespective of which type of correlation metric is used.

Extended Data Figure 5 indicates that the maximum shear strain rates from geodesy show the best correlation and form an upper envelope of wavelength-dependent match to seismicity. The geodynamically predicted rate change of dynamic topography rates also show strong, positive correlation, across most wavelengths  $\geq 200$  km. Moho depth gradients are mainly correlated with seismicity at  $\sim 500$  km wavelengths, indicating that crustal complexities will impose some shorter wavelength modulations on the driving, mantle-based forcing. Finally, GPE gradients appear to contribute with positive correlation values throughout a range of wavelengths, but the total correlation values in Extended Data Fig. 4 are biased by the longest wavelength response, which may be misleading given the relatively small spatial extent of the study region.

Much of the intermountain seismicity band is clustered around Yellowstone itself (Fig. 1a, b), where we would expect shallow volcanic and magmatic processes to complicate any analysis. If we exclude a circular region of  $\sim 200$  km diameter around Yellowstone, total correlations drop by  $\Delta r \approx 0.1$  compared to Extended Data Fig. 4, but relative model performance is again confirmed.

**Multivariable analysis.** Correlation sampling also allows multivariable regression analysis, that is, solving a system of equations

$$Aw = \phi \quad (1)$$

for  $w$ , the ‘importance vector’ with  $n$  dimensions for each of the subset of  $n = 7$  models considered, in a least squares sense.  $\phi$  is the even-area sampled seismicity function with  $m \approx 16,000$  entries where all  $n$  models are defined. (In practice, this covers  $\sim 90\%$  of the region typically captured for Extended Data Fig. 4, leading to slightly different absolute  $r$  values.)  $A$  is  $m$  by  $n$  and holds the  $m$  predictions from the  $n$  models. Each column of  $A$  and  $\phi$  are demeaned and normalized to unity norm before solving equation (1) such that the elements of  $w$ ,  $w_i$ , are comparable in amplitude.

Extended Data Figure 7 shows the solution of equation (1); only the mantle-induced rate of dynamic topography change, GPE, and Moho and  $T_e$  gradients contribute to the non-negative, best-fit solution. The multivariable best fit yields  $r \approx 0.52$  for regular and non-negative least squares, compared to the single,  $r \approx 0.46$ , solution. If we only use the four most important models, the least squares solution is naturally non-negative and also achieves  $r \approx 0.52$ .

An improvement in correlation of  $\Delta r \approx 0.06$  for four compared to a single model is marginal, for example, compared to  $\Sigma_r$ . Part of the reason that no better fit to seismicity can be achieved is that the ‘basis vectors’ are, of course, not orthogonal, and individual models, such as Moho and  $T_e$  gradients, are themselves highly correlated. However, the interpretation of Extended Data Fig. 7 is consistent with a superposition of GPE and structural gradients on the rate change of topography from mantle flow as the main driver.

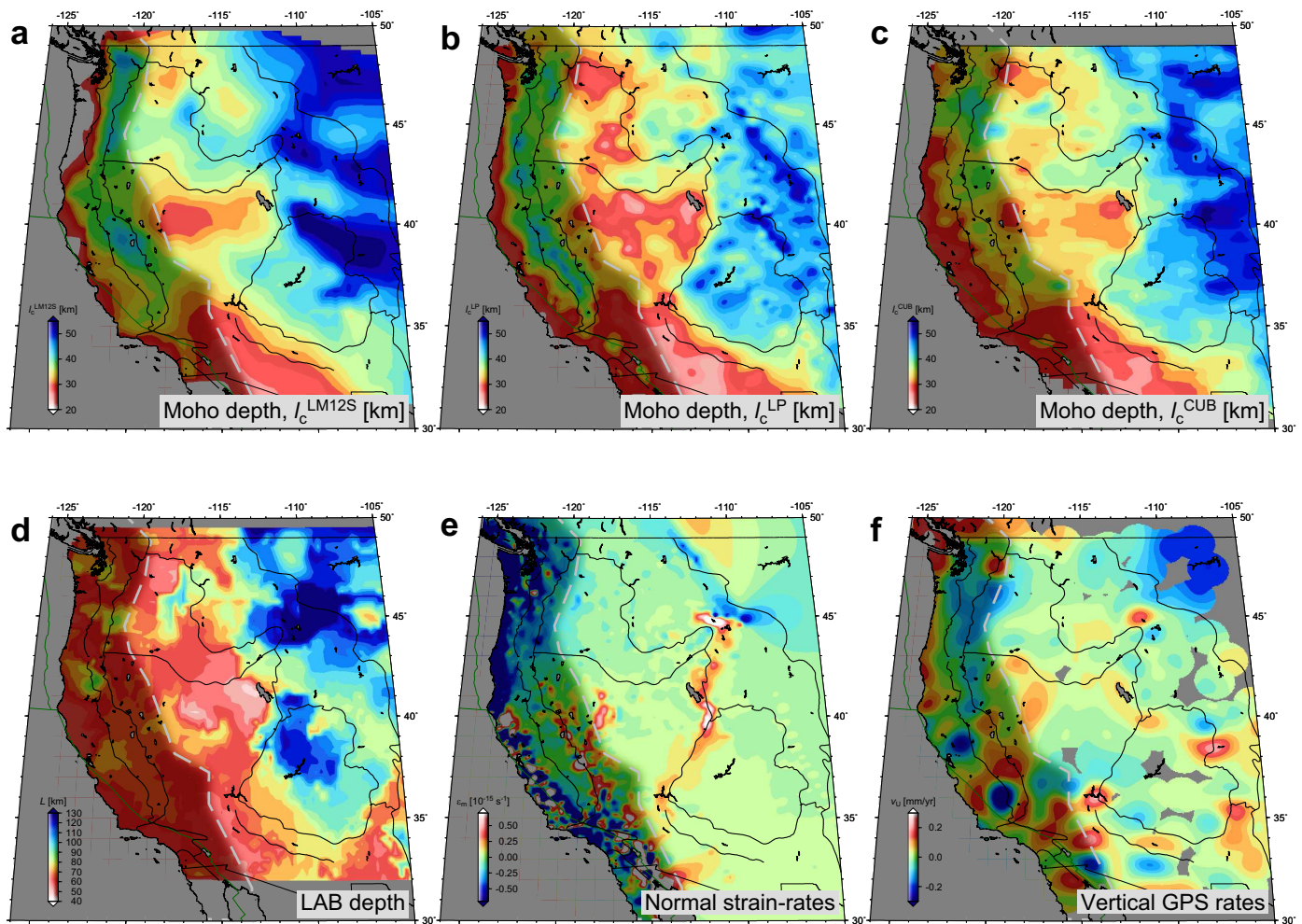
**Comparison with vertical rates from GPS geodesy.** We also evaluated the GPS velocities from the UNAVCO PBO solution (pbo.final\_frame.vel at ftp://data-out.unavco.org/pub/products/velocity/). Extended Data Figure 1f shows a smoothed field constructed from the original vertical velocity estimates after rejection of outliers outside  $\pm$  the RMS of the original data. Compared to the horizontals from GPS, vertical velocities are formally more uncertain, and, more importantly, strongly affected by hydrological, climatic, and anthropogenic signals. While the time series are improving, special processing is still required<sup>45,46</sup>, and we consider distilling the tectonic and possible deep mantle signal from the GPS solutions to be work in progress.

However, initial results from a correlation analysis for regions away from the plate boundary indicate that rate change of dynamic topography from mantle flow shows poor total correlation with GPS verticals (Extended Data Fig. 8), if these are smoothed homogeneously, which may be inappropriate. Rate change of topography from mantle flow is positively correlated with GPS verticals within a band from  $\sim 250$  km to  $\sim 800$  km wavelength, however, similar to the peak of the Moho depth gradient correlation with seismicity in Extended Data Fig. 5. Only dynamic topography from flow, or GPE fields, show total, positive correlations with GPS verticals, and Moho depths are negatively correlated, meaning positive GPS verticals are found preferentially in regions of high GPE and thin crust.

If we compare the GPS verticals with horizontal kinematic constraints, we find that normal strain rates show positive correlation with GPS verticals, across a wide range of wavelengths (Extended Data Fig. 8). Such an association of change of dynamic topography with regions of extension is opposite to what might be expected for an edge-loaded, crustal thickening scenario, and rather more like extension on top of a region that is uplifted because of a basal density anomaly or push. This is consistent with a general expectation that, on scales of  $\lesssim 200\text{--}600$  km (ref. 15), strength of a visco-elasto-plastic lithosphere will partition any applied vertical normal stress primarily into membrane stress rather than uplift.

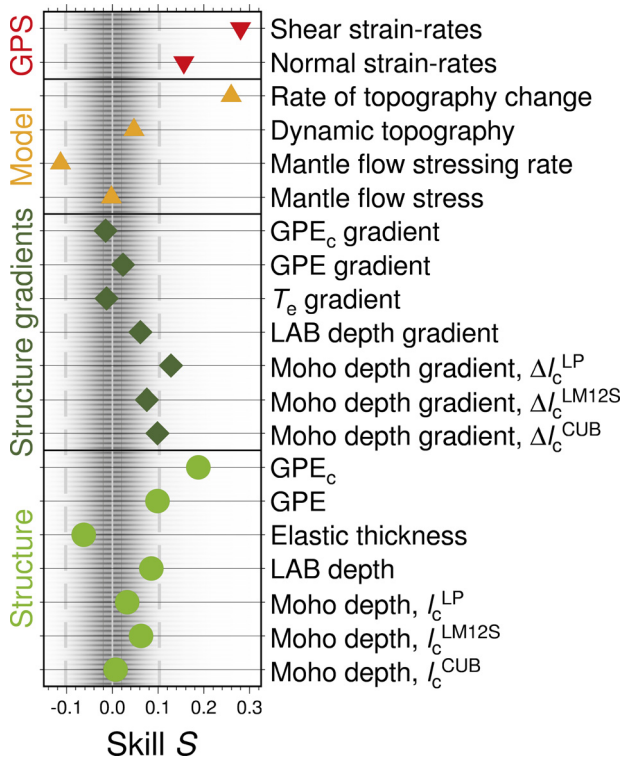
31. Levandowski, W., Jones, C. H., Shen, W., Ritzwoller, M. H. & Schulte-Pelkum, V. Origins of topography in the western U.S.: mapping crustal and upper mantle density variations using a uniform seismic velocity model. *J. Geophys. Res.* **119**, 2375–2396 (2014).
32. Liu, L. & Gurnis, M. Dynamic subsidence and uplift of the Colorado Plateau. *Geology* **38**, 663–666 (2010).
33. Moresi, L. N. & Solomatov, V. S. Numerical investigations of 2D convection with extremely large viscosity variations. *Phys. Fluids* **7**, 2154–2162 (1995).
34. Zhong, S., Zuber, M. T., Moresi, L. & Gurnis, M. Role of temperature-dependent viscosity and surface plates in spherical shell models of mantle convection. *J. Geophys. Res.* **105**, 11063–11082 (2000).
35. Auer, L., Boschi, L., Becker, T. W., Nissen-Meyer, T. & Giardini, D. Savani: a variable-resolution whole-mantle model of anisotropic shear-velocity variations based on multiple datasets. *J. Geophys. Res.* **119**, 3006–3034 (2014).
36. Burov, E. & Guillou-Frottier, L. The plume head-continental lithosphere interaction using a tectonically realistic formulation for the lithosphere. *Geophys. J. Int.* **161**, 469–490 (2005).
37. Braun, J. The many surface expressions of mantle dynamics. *Nature Geosci.* **3**, 825–833 (2010).

38. Becker, T. W. On recent seismic tomography for the western United States. *Geochem. Geophys. Geosys.* **13**, Q01W10 (2012).
39. Schmandt, B. & Humphreys, E. Complex subduction and small-scale convection revealed by body-wave tomography of the western United States upper mantle. *Earth Planet. Sci. Lett.* **297**, 435–445 (2010).
40. Lou, X. & van der Lee, S. Observed and predicted North American teleseismic delay times. *Earth Planet. Sci. Lett.* **402**, 6–15 (2014).
41. Perry, H. K. C., Forte, A. M. & Eaton, D. W. S. Upper-mantle thermochemical structure below North America from seismic-geodynamic flow models. *Geophys. J. Int.* **154**, 279–299 (2003).
42. Moucha, R. *et al.* Deep mantle forces and the uplift of the Colorado Plateau. *Geophys. Res. Lett.* **36**, L19310 (2009).
43. NCEDC. *Northern California Earthquake Data Center: Dataset* (UC Berkeley Seismological Laboratory, 2014).
44. Engdahl, E. R., van der Hilst, R. D. & Buland, R. Global teleseismic earthquake relocation with improved travel times and procedures for depth determination. *Bull. Seismol. Soc. Am.* **88**, 722–743 (1998).
45. Serpelloni, E., Faccenna, C., Spada, G., Dong, D. & Williams, S. D. P. Vertical GPS ground motion rates in the Euro-Mediterranean region: new evidence of velocity gradients at different spatial scales along the Nubia-Eurasia plate boundary. *J. Geophys. Res.* **118**, 6003–6024 (2013).
46. Borsa, A. A., Agnew, D. C. & Cayan, D. R. Ongoing drought-induced uplift in the western United States. *Science* **345**, 1587–1590 (2014).
47. Shen, W., Ritzwoller, M. H. & Schulte-Pelkum, V. Crustal and uppermost mantle structure in the central U.S. encompassing the Midcontinent Rift. *J. Geophys. Res.* **118**, 4325–4344 (2013).
48. Obrebski, M., Allen, R. M., Pollitz, F. & Hung, S.-H. Lithosphere–asthenosphere interaction beneath the western United States from the joint inversion of body-wave traveltimes and surface-wave phase velocities. *Geophys. J. Int.* **185**, 1003–1021 (2011).
49. James, D. E., Fouch, M. J., Carlson, R. W. & Roth, J. B. Slab fragmentation, edge flow and the origin of the Yellowstone hotspot track. *Earth Planet. Sci. Lett.* **311**, 124–135 (2011).

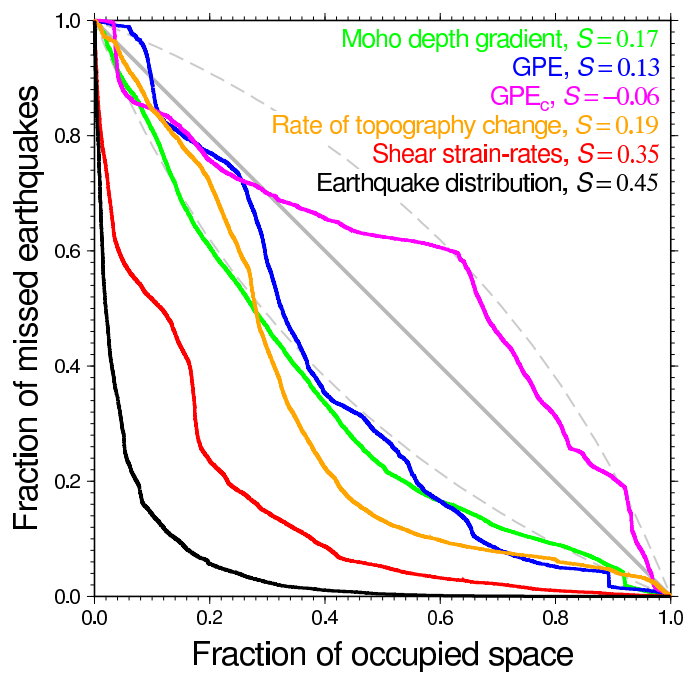


**Extended Data Figure 1 | Maps of selected, additional scalar fields considered for the Molchan analysis in Fig. 2 and Extended Data Fig. 2.** a–c, Moho depth estimates from Levander and Miller<sup>3</sup> (LM12S), Lowry and Pérez-Gussinyé<sup>11</sup> (LP), and Shen *et al.*<sup>47</sup> (CUB). d–f, ‘Lithosphere asthenosphere boundary’ (LAB) depth inferred from receiver functions by

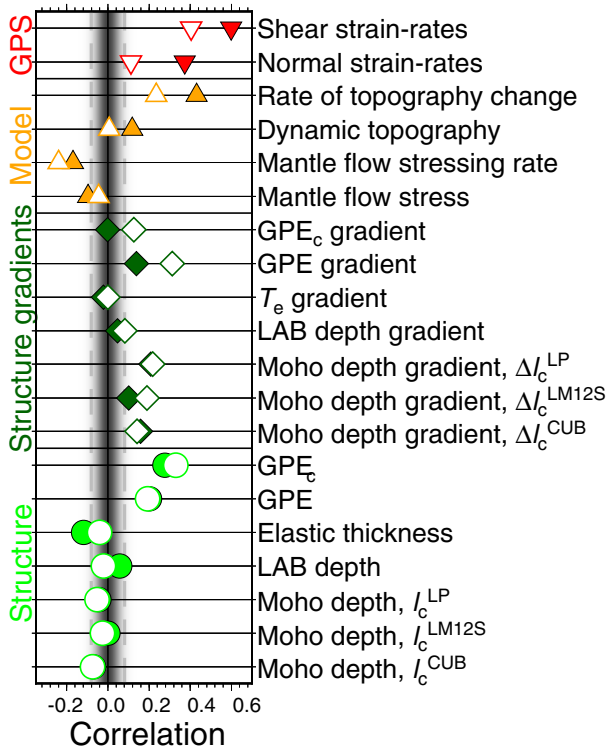
Levander and Miller<sup>3</sup>, shear wave version (d), horizontal normal strain rates based on GPS geodesy from Kreemer *et al.*<sup>29</sup> (extension positive) (e), and vertical GPS rates, smoothed from the 2014 UNAVCO/PBO velocity release (pbo.final\_frame.vel at <ftp://data-out.unavco.org/pub/products/velocity/>) with presumed outliers removed (f).



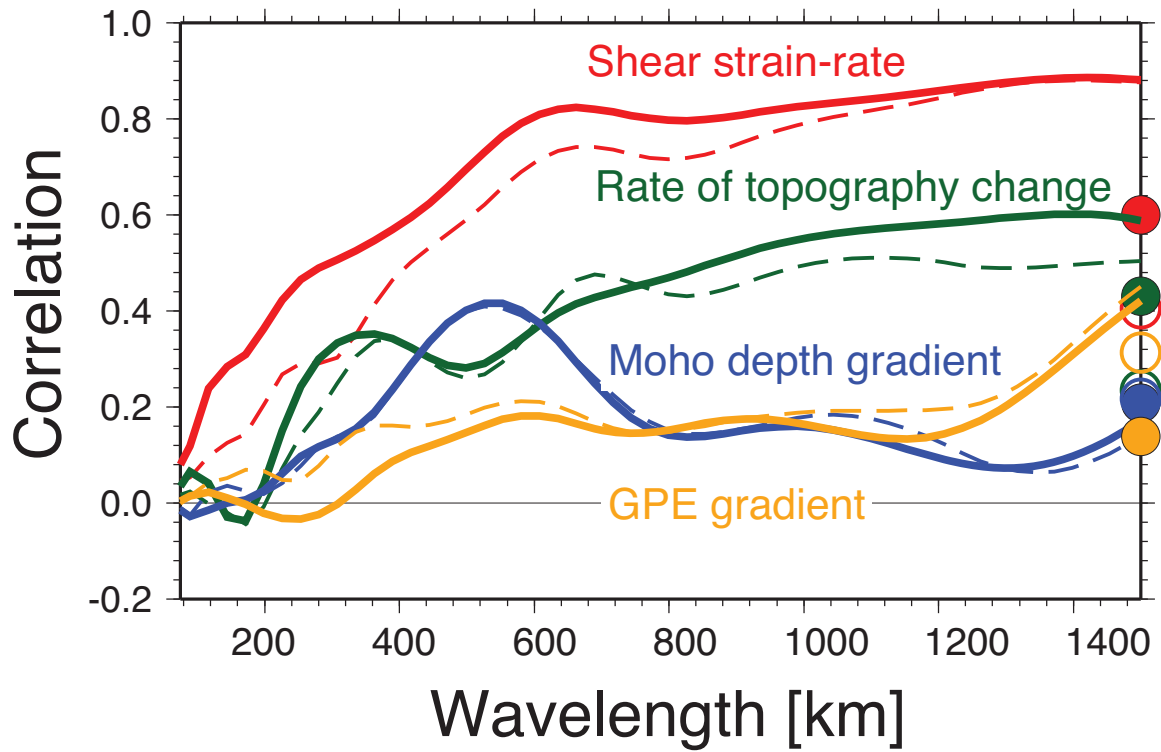
**Extended Data Figure 2 | Molchan skill<sup>20</sup>,  $S$ , for intraplate seismicity for an expanded set of models.** We show results for three Moho models: CUB<sup>47</sup>, LM12S<sup>3</sup> (S wave version) and LP<sup>11</sup> (as used in the main text, compare Extended Data Fig. 1a–c), estimates of LAB thickness from receiver functions (Extended Data Fig. 1d) and elastic thickness, and two kinds of GPE models, as in the main text, gradients thereof, geodynamic model predictions, and kinematic models for the western United States (Fig. 1). Dashed lines indicate the regions outside of which results are 95% significant. This more comprehensive analysis confirms the conclusions about relative model performance.



**Extended Data Figure 3 | Molchan error curves for prediction of all seismicity in the entire region of Fig. 1b.** Compare with Fig. 2a, which only considers seismicity outside the plate boundary zone as indicated in Fig. 1. Rate change of dynamic topography shows significant positive skill, even when including plate boundary seismicity.

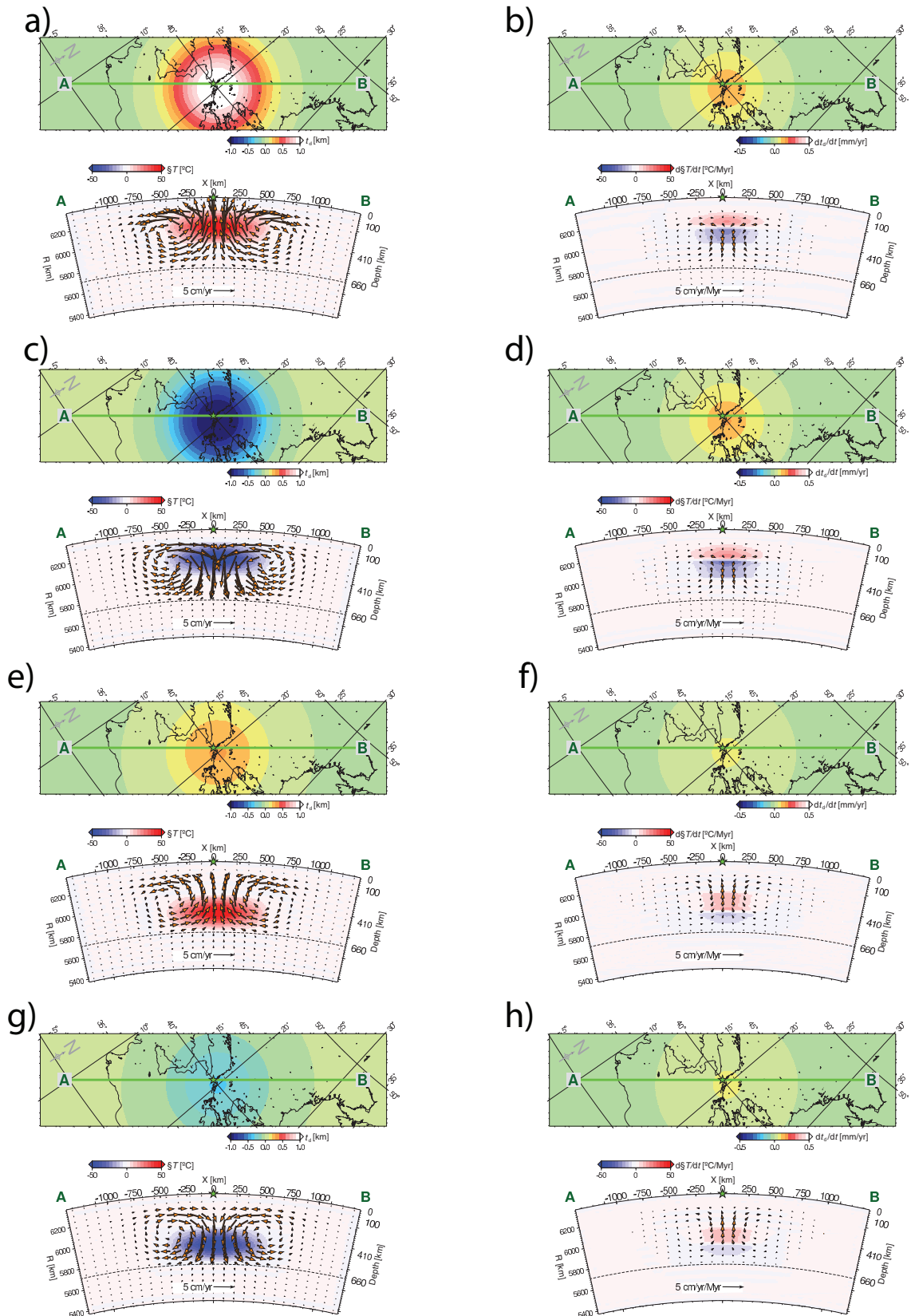


**Extended Data Figure 4 | Correlation,  $r$ , between seismicity density ( $\phi$ , Fig. 1b) and different models.** Obtained by even-area sampling of regions outside the plate boundary zone in Fig. 1, compare with Extended Data Fig. 2. Filled and open symbols are for linear (Pearson),  $r$ , and Spearman rank,  $r_s$ , correlation, respectively. Dashed lines indicate the regions outside of which results are 95% significant, grey shading denotes approximate random density function distribution. Relative performance of Pearson correlation is consistent with results for skill (Extended Data Fig. 2), and Spearman rank shows some deviations, indicating lack of simple, linear relationships between  $\phi$  and scalar fields.



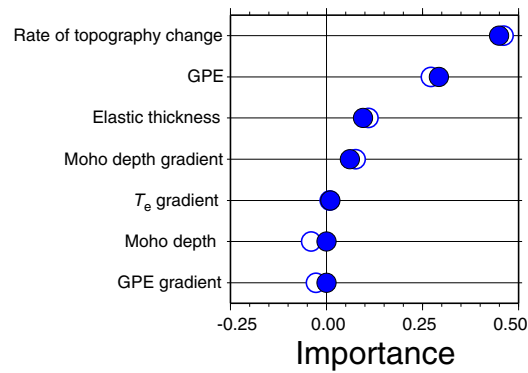
**Extended Data Figure 5 | Wavelength-dependent correlation of seismicity and selected scalar fields.** Models considered: shear strain rates from geodesy (Fig. 1c); rate change of dynamic topography (Fig. 1f); gradients of Moho depth<sup>11</sup>; and GPE (Fig. 1d). Circles on right show the total correlation as in Extended Data Fig. 4. Solid, heavy lines and filled symbols are for linear (Pearson) correlation, and thin, dashed lines and open symbols are for

Spearman rank correlation, respectively. Rate change of dynamic topography shows positive correlation with seismicity across most wavelengths. Shorter wavelengths, where the response of a rheologically complex lithosphere will be most relevant, emphasize the differences between  $r$  and  $r_s$  seen in Extended Data Fig. 4.



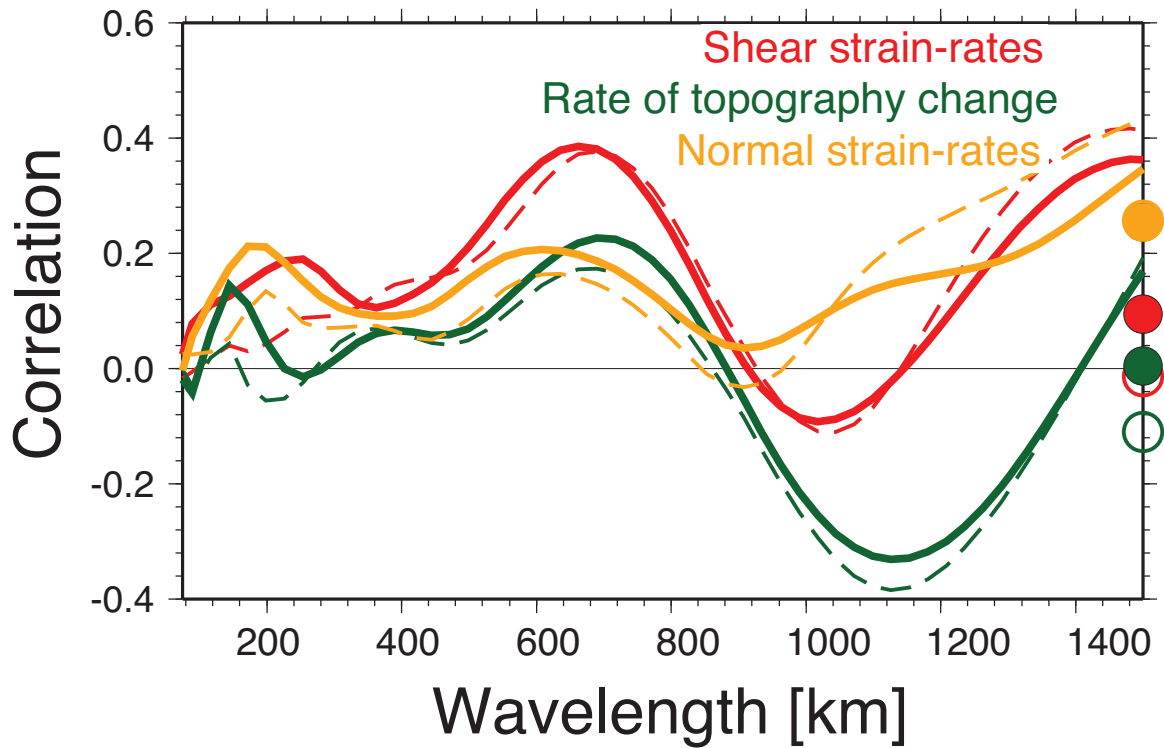
**Extended Data Figure 6 | Illustrative, synthetic mantle flow models exploring dynamic topography and rate change thereof for simple, *ad hoc* temperature anomalies.** a–h, Bottom subplots show temperature anomalies and mantle flow velocities, top subplots show dynamic topography on the surface (left) and temporal change thereof (right) for four mantle density cases

along profiles. a, b, Shallow, hot anomaly; c, d, shallow, cold anomaly; e, f, deep, hot anomaly; g, h, deep, cold anomaly. Note how rate change of dynamic topography is positive for both cold, sinking and hot, rising anomalies because of reduction of negative and increase of positive dynamic topography, respectively<sup>23,24</sup>.



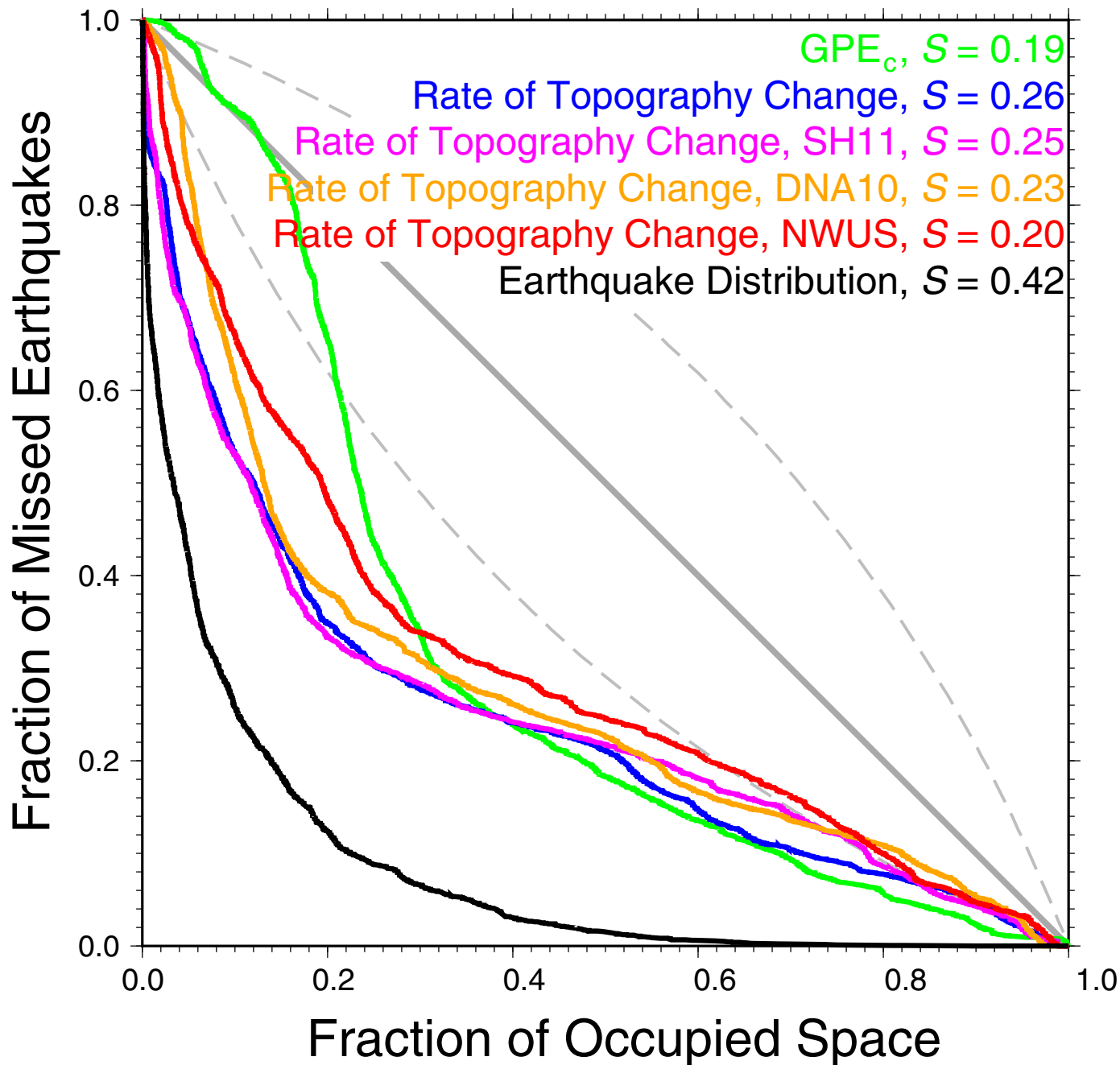
**Extended Data Figure 7 | Multivariable regression analysis to best fit the seismicity density, evaluating a subset of the models of Extended Data Fig. 4.** The normalized contribution of each model vector, the importance  $w_i$ , is indicated by filled and open symbols from a non-negative or regular least

squares solution of equation (1), respectively. Results indicate that rate change of dynamic topography is the strongest driver of seismicity, with contributions from GPE, and modulated by Moho depth gradients and elastic thickness variations (compare with Extended Data Fig. 4).



**Extended Data Figure 8 | Wavelength-dependent correlation between vertical GPS rates (Extended Data Fig. 1f) and selected scalar fields.** For models and legend see Extended Data Fig. 5. Rate of topography change and shear strain rates show positive correlation with geodetically imaged uplift at wavelengths of  $\sim 500\text{--}900$  km, but rate change of dynamic topography is

negatively correlated at longer wavelengths. Results indicate that rate change of dynamic topography may need to be understood more fully in context of a rheologically realistic model of lithospheric deformation, whereas geodetic uplift rates may be strongly affected by other signals, for example, climatic and hydrological.



**Extended Data Figure 9 | Molchan curves for mantle flow predictions for a range of tomographic models.** Flow modelling uses our reference model<sup>12</sup> (compare with Fig. 2a and Extended Data Fig. 2), and older tomography<sup>38</sup>: SH11 (ref. 39) is a precursor of ref. 12; DNA10 a joint surface and body wave inversion by Obrebski *et al.*<sup>48</sup>; and NWUS-S an earlier, USArray-based shear

wave tomography model by James *et al.*<sup>49</sup>. The best GPE model and smoothed seismicity are shown for reference. Older tomographic models substantiate our conclusions based on ref. 12; in particular SH11, which was found to best predict delay times<sup>40</sup>, has near-identical skill.